Proceedings of the 9th World Congress on Momentum, Heat and Mass Transfer (MHMT'24)
London, United kingdom – April 11 – 13, 2024
Paper No. ENFHT 279
DOI: 10.11159/enfht24.279

The Multi-Node Moving Boundary Model for Transient Dynamics of A Typical Counter-Current Steam Generator Using Python Programming

A.Fakhraei[1], Farshad Faghihi[1]
School of Mechanical Eng., Shiraz University, Shiraz 71936-16548, Iran

Abstract **-** We derived the formulation and methodology of CFD for the counter-current steam generator, highlighting the presence of several fluid phases, different heat transfer regimes, and different media. This research proposes a model based on the multi-node moving boundary model for analysing transient problems occurring in a typical case study helically coiled tube once-through counter-current steam generator. This model comprises three moving boundary regions, each inclusive of several nodes. Several transient cases are considered to evaluate the model's performance, and the results are benchmarked using the worldwide known RELAP5 code. Python programming language and its necessary packages, such as Scipy, Numpy, matplotlib, pandas, pyXSteam and scikit-fuzzy, are utilized for simulations is developed herein.

Keywords**:** CFD of SG's Moving Boundary Model, Counter-current Steam Generator Dynamics, Helical Coil Steam Generator, Python code programming.

1. Introduction

Most operating current commercial nuclear power plants utilize designs in which the primary fluid flows through tubes and transfers heat with the secondary side tubes such as U-Tubes SGs or the Russian-type horizontal SG designs (Atomenergoproekt, 2015; Lee et al., 1980; Westinghouse, 2011). But, one of the most efficient, and new design, is the *counter-current flow helically-coiled* steam generator. Counter-current flow steam generators operate on the principle of heat exchange between two separate loops of fluids moving in the opposite directions. On the secondary side, feedwater enters the steam generator through the feedwater inlet and passes through the region between the tube bundle wrapper and the shell. The feedwater absorbs heat from the primary flow through the tubes. The subcooled feedwater flow becomes a two-phase mixture along the vertical axis, and then fluid moves up through the spiral vanes and becomes the super-heat fluid.

Nowadays, a few PWR reactors such as NuScale, IRIS, and CAREM-25 have successfully employed counter-current SGs that are helically coiled SGs and have been identified as the superior option for heat transfer from the primary to the secondary side. Compared to U-Tube SGs, which are currently utilized in commercial Pressurized Water Reactors, Helical Coil Steam Generators (HCSGs) offer several advantages such as compact design, higher heat transfer efficiency, and the ability to superheat the outlet fluid.

There are two approaches to the fluid dynamics modelling of the HCSGs. The first approach involves using the finite volume method with fixed boundaries. This method requires a large number of fine nodes to detect the boundaries of each phase and their respective characteristics. The second approach involves utilizing a moving boundary model with coarse nodes. This approach tracks the boundary of phases using a specially formulated method, obviating the need for fine nodes. Studies by Kerlin, Secker, and Gilbert have shown that a movable boundary model is more computationally efficient for HCSGs (Kerlin, 1976; Secker and Gilbert, 1975).

(Tzanos, 1988a, b) developed a movable boundary model for a Liquid Metal Fast Breeder Reacor (LMFBR). This work resulted in the creation of a computer code-named STEGA, which was capable of simulating the behaviour of LMFBR OTSG. The model utilized different heat transfer models for nucleate and film boiling regions, and the equations were solved using a semi-analytic method for steady-state conditions. The Gear method implemented in the LSODE package for stiff differential equations was used to integrate differential equations for the transient solution. The proposed approach was benchmarked against the ETEC shutdown experiment carried out with the PSM-W numerical code (Berry, 1983) under transient condition.

(Jensen and Tummescheit, 2002) developed a 7th-order model for a multi-phase heat exchanger's system and controller design. This model utilized the slip ratio to calculate the mean average void fraction in the two-phase section and applied

Leibnitz's rule to convert governing PDE equations to a set of ODEs.(Arda and Holbert, 2015, 2016) developed a model that simulates the response of the typical counter-current steam generator transient conditions. This model consisted of ten state variables, including secondary pressure, subcooled and two-phase heights, three node temperatures in the primary system, node temperature of the tube metal in each region, and subcooled and superheat enthalpies. Results from this work showed significant deviation from the reactor's design data. Additionally, the primary side equations developed in this work lacked some terms relevant to the boundary length of phases.

(Zhang et al., 2017) developed a numerical computer code called THAOT for performance analysis and design of H-OTSGs in SMRs. In this research, the steady-state condition of HCSG has been focused on. The HCSG has been divided into subcooled, saturated, post-dry-out, and superheat sections. For each region, its proper empirical correlation has been used for heat transfer characteristics. The code is used to obtain MRX steam generator thermal-hydraulic features, and results are benchmarked with calculated data.

In their recent research, (Wu et al., 2022) utilized a fully implicit Jacobian-free Newton-Krylov algorithm to solve a moveable boundary model with eight state variables. They conducted a comparative analysis of the results obtained for the HTR-10 steam generator with those obtained using a fine mesh approach, which was previously presented (Wu et al., 2021). The computational efficiency of the novel moving boundary model developed in their study was found to be satisfactory, while the fine mesh approach demonstrated superior accuracy.

The primary goal of this study is to develop an accurate and efficient model for simulation of a typical case-study helically-coiled counter-current SG including 54 ODEs. This model takes advantage of both moving boundary models and fine mesh approaches by detecting the boundary of the phases and also the capability to have each region divided into several computational nodes. Additionally, we aimed to design a computer Python programming and its necessary packages such as Scipy, Numpy, matplotlib, pandas, pyXSteam, and scikit-fuzzy are utilized to carry out the code programming of the research. The developed code has been benchmarked with our previous RELAP5 studies on the mentioned case study (Fakhraei et al., 2020; Fakhraei et al., 2021; Fakhrarei et al., 2021). Moreover, the developed model was fine validated against the published design data. The Python programming language and its necessary packages, such as Scipy, Numpy, matplotlib, pandas, pyXSteam and scikit-fuzzy, are utilized for simulations, to solve ODEs, optimization and controlling.

2. Methodology of the Research

2.1 CFD Modeling Approach

First, we should import the 3D geometry of the steam generator, and ensure that the geometry is properly scaled and aligned. Then one should create a mesh that accurately represents the geometry and employ a structured or unstructured grid approach depending on the complexity of the system. Assign appropriate boundary conditions including define inlet and outlet conditions for steam and coolant streams and specify the tubes conditions such as temperature and heat transfer coefficients.

2.2 Defining the Problem and Mathematical formulation of the HCSG

In this research, the model is formulated to track the boundaries of the subcooled, two-phase, and superheat regions. Furthermore, each region can be divided into several nodes, with the node lengths in the primary system and tube metals varying according to their corresponding secondary nodes. The mathematical formulation for the secondary side is based on mass and energy balance equations, while only energy balance equations are required for the tube metal section and primary side. The following assumptions have been made:

- Uniform secondary pressure,
- One-dimensional flow,
- Negligible axial heat conductivity,
- No phase-change in the primary side,
- One *equivalent* helically-coiled tube in the SG.

Figure 1 shows the schematic diagram of the implemented model for HCSG. The subcooled boundary extends from the secondary feedwater inlet to the point that fluid reaches the saturated enthalpy $(h \leq h_f)$ while two-phase boundaries placed

between the steam quality of $(0 < x < 1)$ and superheat section $(h > h_g)$. Each region consists of numbers of nodes with the same lengths. In other words, it is considered $\Delta l = l_{j+1} - l_j = const$, $\Delta s = s_{j+1} - s_j = const$ and $\Delta v = v_{j+1} - v_j = const$. In which l, s, v is defined as

$$l = \frac{z}{Z_S},\ s = \frac{Z - Z_S}{Z_T - Z_S},\ v = \frac{Z - Z_T}{Z_{SG} - Z_T} \qquad 1$$

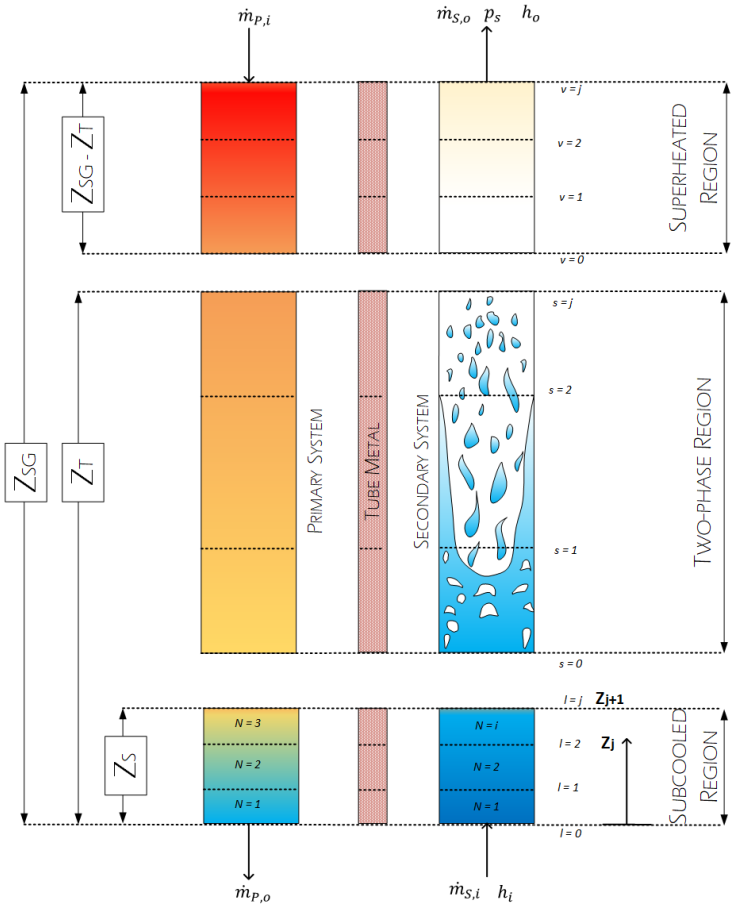

Figure 1: Schematic of the three regions and movable boundaries in each region.

Table 1: length and its time-derivative in different regions of SGs (c.f. Fig. 1)

Region	Z_{j+1}	$(Z_{j+1} - Z_j)$	dZ_{j+1}/dt
Subcooled	$l_i Z_S$	$\Delta l Z_S$	$l_i\, dZ_S/dt$
Two-phase	$Z_S + s_i(Z_T - Z_S)$	$\Delta s(Z_T - Z_S)$	$dZ_S/dt + s_i(dZ_T/dt - dZ_S/dt)$
Superheat	$Z_T + v_i(Z_{SG} - Z_T)$	$\Delta v(Z_{SG} - Z_T)$	$dZ_T/dt\,(1 - v_i)$

2.2.1 Primary side of HCSG

The energy conservation equation for the primary side can be written as follows:

$$\frac{\partial(\rho h)}{\partial t}+\frac{\partial(Gh)}{\partial x}=\frac{Q}{A}+\frac{\partial P}{\partial t} \quad (2)$$

By applying Leibnitz's rule, the PDE in equation 2 can be transformed into an ODE. Leibnitz's rule can be mathematically expressed as:

$$\frac{d}{dt}\int_{z_1}^{z_2} f(z,t)dz = f(z_2,t)\frac{dz_2}{dt}-f(z_1,t)\frac{dz_1}{dt}+\int_{z_1}^{z_2}\frac{\partial f(z,t)}{\partial t}dz \quad (3)$$

The energy equation for the primary side of the steam generator can be derived by integrating equation 2 over the volume and applying Leibnitz's rule.

$$\rho C_p A_{pr}\left[(Z_{j+1}-Z_j)\frac{d\bar{T}_i}{dt}+(\bar{T}_i-\bar{T}_{i+1})\frac{dZ_{j+1}}{dt}\right] = n\pi D_o\alpha_o L_i(\bar{T}_{wi}-\bar{T}_{pi})+\dot{m}_p C_p(\bar{T}_{i+1}-\bar{T}_i) \quad (4)$$

The upwind approximation is utilized to determine the parameters' value at the node boundaries to avoid irrational results (Patankar, 2018). The intermediate steps involved in this process are elaborated in the article's appendix. By substituting Z_j for boundaries of the nodes and their derivative dZ_{j+1}/dt from Table 1 the final equation for each node can be obtained. The primary side heat transfer coefficient is computed using the Zukauskas correlation, which is applicable for crossflow across a staggered array of tubes for Reynolds numbers ranging from $10 < Re < 10^6$ and Prandtl numbers between $0.7 < Pr < 500$ (Žukauskas, 1972).

$$\alpha_o = 0.35\frac{k}{d}Re_{d,max}^{0.6}Pr^{0.36}\left(\frac{Pr}{Pr_w}\right)^{1/4} \quad (5)$$

In this formulation, the Prandtl number denoted as Pr_w, is evaluated at the wall temperature.

2.2.2 Tube metal heat transfer

The energy balance equation for the tube metal nodes can be derived using:

$$C_w\rho_w A_w\frac{dT_w}{dt}=n\pi\alpha_i D_i(T_s-T_w)+n\pi\alpha_o D_o(T_p-T_w) \quad (6)$$

Integration over Z_{j+1} to Z_j and applying Leibnitz's rule gives

$$C_w\rho_w A_w\left[(Z_{j+1}-Z_j)\frac{d\bar{T}_{w(i)}}{dt}+\frac{(\bar{T}_{w(i)}-\bar{T}_{w(i+1)})}{2}\frac{dZ_{j+1}}{dt}+\frac{(\bar{T}_{w(i-1)}-\bar{T}_{w(i)})}{2}\frac{dZ_j}{dt}\right] = n\pi\alpha_i D_i(Z_{j+1}-Z_j)(\bar{T}_{s(i)}-\bar{T}_{w(i)})+n\pi\alpha_o D_o(Z_{j+1}-Z_j)(\bar{T}_{p(i)}-\bar{T}_{w(i)}) \quad (7)$$

The above equation is obtained with the assumption that the temperature of the tubes at the boundaries to be average of two adjacent nodes. In another word $\bar{T}_{w(j+1)}=\frac{(\bar{T}_{w(i)}+\bar{T}_{w(i+1)})}{2}$ and $\bar{T}_{w(j)}=\frac{(\bar{T}_{w(i)}+\bar{T}_{w(i-1)})}{2}$. Replacing lengths and their derivatives from Table 1 in Equation 7 gives the final form of the equation for each node.

2.2.3 Secondary side heat and flow transfer

In order to calculate the secondary system dynamics, mass, and energy balance equations are needed to be solved for each node. These equations are expressed as:

$$\frac{\partial \rho}{\partial t} + \frac{\partial \rho u}{\partial z} = 0 \tag{8}$$

$$\frac{\partial (\rho h - P)}{\partial t} + \frac{\partial (\rho u h)}{\partial z} = \frac{Q}{A} \tag{9}$$

Multiplying Equations 8 and 9 to steam generator tubes flow cross-section, integrating over Z_{j+1} to Z_j, using Leibnitz's rule and upwind approximation the above equations transform to

Mass balance:

$$A_s \left[(Z_{j+1} - Z_j) \frac{d\bar{\rho}_i}{dt} + (\bar{\rho}_{i-1} - \bar{\rho}_i) \frac{dZ_j}{dt} \right] = \dot{m}_{Z_j} - \dot{m}_{Z_{j+1}} \tag{10}$$

Energy balance:

$$A_s \left[(Z_{j+1} - Z_j) h_i \frac{d\bar{\rho}_i}{dt} + (Z_{j+1} - Z_j) \rho_i \frac{dh_i}{dt} - (Z_{j+1} - Z_j) \frac{dP_i}{dt} + (\rho_{i-1} h_{i-1} - \rho_i h_i) \frac{dZ_j}{dt} \right] = \dot{m}_{i-1} h_{i-1} - \dot{m}_i h_i + n\pi D_i \alpha_i (Z_{j+1} - Z_j)(\bar{T}_{w(i)} - \bar{T}_{s(i)}) \tag{11}$$

To satisfy the constraint that unknown variables must be equivalent to the equation numbers, the time derivative of the density must be linked to the system pressure and enthalpy in the subcooled and superheat sections, or the pressure and void fraction in the two-phase region. For each region the values for $d\bar{\rho}_i/dt$, dZ_j/dt, dh_i/dt is interpreted differently. In the subsequent sections, each region is explained separately. For the sake of consistency in notations, we consider j+1 to be equal to i.

2.2.3.1 Subcooled region

Density in the subcooled region can be expressed as a function of pressure and enthalpy. So, the term $d\bar{\rho}_i/dt$ in the subcooled section can be related to pressure and enthalpy by

$$\frac{d\bar{\rho}_i}{dt} = \frac{\partial \rho_i}{\partial P_s}|_h \frac{dP_s}{dt} + \frac{\partial \rho_i}{\partial h_i}|_{P_s} \frac{dh_i}{dt} \tag{12}$$

At the final node of the subcooled section, the fluid attains the saturation temperature. The saturation enthalpy can be expressed solely as a function of pressure.

$$\frac{d\rho_i}{dt} = \left(\frac{\partial \rho_f}{\partial P_s} + \frac{\partial \rho_f}{\partial h_f} \frac{\partial h_f}{\partial P_s} \right) \frac{dP_s}{dt} \tag{13}$$

In this study, the values of partial derivatives at each time step are computed and updated using the steam table. Replacing the subcooled length from Table 1 and combining equations 11, 12, and 13, the mass balance equation for nodes before saturation node becomes

$$A_s \left[\Delta l Z_S \left(\frac{\partial \bar{\rho}_i}{\partial P_s}|_h \frac{dP_s}{dt} + \frac{\partial \bar{\rho}_i}{\partial \bar{h}_i}|_{P_s} \frac{d\bar{h}_i}{dt} \right) + l_{i-1} (\bar{\rho}_{i-1} - \bar{\rho}_i) \frac{dZ_S}{dt} \right] = \dot{m}_{i-1} - \dot{m}_i \tag{14}$$

Also, the mass balance for the saturation node can be expressed as:

$$A_s\left[\Delta l Z_S\left(\frac{\partial \rho_f}{\partial P_s}+\frac{\partial \rho_f}{\partial h_f}\frac{\partial h_f}{\partial P_s}\right)\frac{dP_s}{dt}+l_{i-1}(\bar{\rho}_{i-1}-\bar{\rho}_i)\frac{dZ_S}{dt}\right]=\dot{m}_{i-1}-\dot{m}_i \quad (15)$$

With the same approach energy balance for pre-saturated nodes become

$$A_s\left[\Delta l Z_S\bar{h}_i\left(\frac{\partial \bar{\rho}_i}{\partial P_s}|_h\frac{dP_s}{dt}+\frac{\partial \bar{\rho}_i}{\partial \bar{h}_i}|_{P_s}\frac{d\bar{h}_i}{dt}\right)+\Delta l Z_S\bar{\rho}_i\frac{d\bar{h}_i}{dt}-\Delta l Z_S\frac{dP_i}{dt}+l_{i-1}(\bar{\rho}_{i-1}\bar{h}_{i-1}-\bar{\rho}_i\bar{h}_i)\frac{dZ_S}{dt}\right]=\dot{m}_{i-1}\bar{h}_{i-1}-\dot{m}_i\bar{h}_i+n\pi D_i\alpha_i\Delta l Z_S(\bar{T}_{w(i)}-\bar{T}_{s(i)}) \quad (16)$$

For the saturation node, this equation takes the form

$$A_s\left[\Delta l Z_S\bar{h}_i\left(h_i\frac{\partial \bar{\rho}}{\partial P_s}|_{h_i}-1+\left(h_i\frac{\partial \bar{\rho}}{\partial h}|_{P_s}+\bar{\rho}_i\right)\frac{\partial h_f}{\partial P_s}\right)\frac{dP_s}{dt}+\Delta l Z_S\bar{\rho}_i\frac{d\bar{h}_i}{dt}+l_{i-1}(\bar{\rho}_{i-1}\bar{h}_{i-1}-\bar{\rho}_i\bar{h}_i)\frac{dZ_S}{dt}\right]=\dot{m}_{i-1}\bar{h}_{i-1}-\dot{m}_i\bar{h}_i+n\pi D_i\alpha_i\Delta l Z_S(\bar{T}_{w(i)}-\bar{T}_{s(i)}) \quad (17)$$

The heat transfer coefficient in the subcooled and also superheated region is calculated using the Gnielinski correlation for fully developed turbulent flow in smooth tubes (Gnielinski, 1976).

$$Nu=0.0214(Re^{0.8}-100)Pr^{0.4} \quad (18)$$

This correlation is valid for $0.5<Pr<1.5$ and $10^4<Re<5\times10^6$.

2.2.3.2 Two-phase region

In the two-phase region fluid density can be related to the void fraction using

$$\rho_i=\rho_f+\alpha\rho_{fg} \quad (19)$$

Differentiating from equation 19 gives

$$\frac{d\rho_i}{dt}=\rho_{fg}\frac{d\alpha_i}{dt}+\alpha_i\frac{d\rho_{fg}}{dt}+\frac{d\rho_f}{dt} \quad (20)$$

The time derivative of the saturation densities can be related to the system pressure using the chain rule.

$$\frac{d\rho_i}{dt}=\rho_{fg}\frac{d\alpha_i}{dt}+\left(\alpha_i\frac{d\rho_{fg}}{dP_s}+\frac{d\rho_f}{dP_s}\right)\frac{dP_s}{dt} \quad (21)$$

Combining equations 10, 21, length, and its derivatives for the two-phase section from Table 1, the mass conservation equation for the two-phase becomes

$$A_s\Delta s(Z_T-Z_S)\rho_{fg}\frac{d\alpha_i}{dt}+A_s\Delta s(Z_T-Z_S)\left(\alpha_i\frac{d\rho_g}{dP_s}+(1-\alpha_i)\frac{d\rho_f}{dP_s}\right)\frac{dP_s}{dt}+A_s\rho_{fg}(\alpha_{i-1}-\alpha_i)(1-s_{i-1})\frac{dZ_S}{dt}+A_s\rho_{fg}(\alpha_{i-1}-\alpha_i)s_{i-1}\frac{dZ_T}{dt}=\dot{m}_{i-1}-\dot{m}_{\mathrm{i}} \quad (22)$$

With the same approach, the energy balance can be written

$$A_s \Delta s (Z_T - Z_S)(\rho_g h_g - \rho_f h_f)\frac{d\alpha_i}{dt} + A_s \Delta s (Z_T - Z_S)\left(\alpha_i \rho_g \frac{dh_g}{dP_s} + \alpha_i h_g \frac{d\rho_g}{dP_s} + (1-\alpha_i)\left(\rho_f \frac{dh_f}{dP_s} + h_f \frac{d\rho_f}{dP_s}\right) - 1\right)\frac{dP_s}{dt} + A_s \rho_{fg}(\alpha_{i-1} - \alpha_i)(1 - s_{i-1})\frac{dZ_S}{dt} + A_s \rho_{fg}(\alpha_{i-1} - \alpha_i)s_{i-1}\frac{dZ_T}{dt} = m_{i-1}h_{i-1} - m_i h_i + n\pi D_i \alpha_i \Delta s (Z_T - Z_S)(T_{Mi} - T_{si}) \quad (23)$$

2.2.3.3 Heat transfer coefficient for saturated boiling

Heat transfer for saturated boiling is calculated using the Chen correlation (Chen, 1966; Todreas and Kazimi, 2012). In this approach, convection coefficient is the combination of nucleate boiling and convective parts. This correlation is valid for saturated boiling in pressures between 0.17 MPa to 3.5 MPa with flow velocity from 0.06 m/s to 4.5 m/s and heat fluxes smaller than 2.4 MW/m2.

$$h_{sat} = h_c + h_{NB} \quad (24)$$

The convective part of the convection coefficient can be calculated based on a modified Dittus-Bolter correlation that can be expressed as:

$$h_c = 0.023\left(\frac{G(1-x)D_e}{\mu_f}\right)^{0.8}\left(Pr_f\right)^{0.4}\frac{k_f}{D_e}F \quad (25)$$

The parameter F in this formula has been taken into account due to enhanced heat transfer as a result of the presence of vapor and its respective turbulence. This term can be approximated by:

$$F = 1 \text{ for } \frac{1}{X_{tt}} < 0.1 \quad (26)$$

$$2.35\left(0.213 + \frac{1}{X_{tt}}\right)^{0.736} \text{ for } \frac{1}{X_{tt}} > 0.1 \quad (27)$$

In which

$$\frac{1}{X_{tt}} = \left(\frac{x}{1-x}\right)^{0.9}\left(\frac{\rho_f}{\rho_g}\right)^{0.5}\left(\frac{\mu_g}{\mu_f}\right)^{0.1} \quad (28)$$

Also, the nucleation part in equation 1 is based on the Forster-Zuber equation that can be written as:

$$h_{NB} = S\left[\frac{(k^{0.79}c_p^{0.45}\rho^{0.49})_f}{\sigma^{0.5}\mu_f^{0.29}h_{fg}^{0.24}\rho_g^{0.24}}\right]\Delta T_{sat}^{0.24}\Delta P^{0.75} \quad (29)$$

where in this equation $\Delta T_{sat} = T_W - T_{sat}$; $\Delta p = p(T_W) - p(T_{sat})$ and S can be written as

$$S = \frac{1}{1 + 2.53 \times 10^{-6} Re^{1.17}} \quad (30)$$

where $Re = Re_l F^{1.25}$ and $Re_l = \frac{G(1-x)D}{\mu_l}$

2.2.3.4 Heat transfer for the post-dry-out region

The post-dry-out heat transfer is considerably lower than that in the saturated boiling region, and this phenomenon has a significant impact on the solution. To address this issue, the Levitan and Borevskiy correlation (Lee and Chang, 2008) has been employed in this study. For steam quality greater than

$$x_{ad} = 2.7\left(\frac{\rho_l \sigma}{G^2 d}\right)^{1/4}\left(\frac{\rho_v}{\rho_l}\right)^{1/3} \quad (31)$$

post-dry-out heat transfer correlation is used. Leveraging the following equation

$$\alpha_{ad} = \frac{\gamma x_{ad}}{1 + x_{ad}(\gamma - 1)} \quad (32)$$

the void fraction at which dry-out takes place can be calculated. For the sub-nodes in the two-phase section with a void fraction higher than α_{ad}, Chen and Chen heat transfer correlation is used

$$h_c = 0.175\frac{k_{v,f}}{D}\left(\frac{\rho_{v,f} u_v D}{\mu_{v,f}}\right)^{0.812} Pr_{v,f}^{0.33} F \quad (33)$$

With

$$F = 2.32(1 + 0.1P)exp(-12x) + 1 \quad (34)$$

P in this correlation is pressure in MPa.

2.2.3.5 Superheat region

Equation 12 is valid for the superheated section. Substituting superheat region length and derivative, the conservation of the mass for this region becomes

$$A_s\left[\Delta v(Z_{SG} - Z_T)\left(\frac{\partial \bar{\rho}_i}{\partial P_s}|_h \frac{dP_s}{dt} + \frac{\partial \bar{\rho}_i}{\partial \bar{h}_i}|_{P_s} \frac{d\bar{h}_i}{dt}\right) + (1 - v_{i-1})(\bar{\rho}_{i-1} - \bar{\rho}_i)\frac{dZ_T}{dt}\right] = \dot{m}_{i-1} - \dot{m}_i \quad (35)$$

With the same approach, the energy balance can be written

$$A_s\left[\Delta v(Z_{SG} - Z_T)\bar{h}_i\left(\frac{\partial \bar{\rho}_i}{\partial P_s}|_h \frac{dP_s}{dt} + \frac{\partial \bar{\rho}_i}{\partial \bar{h}_i}|_{P_s} \frac{d\bar{h}_i}{dt}\right) + \Delta v(Z_{SG} - Z_T)\bar{\rho}_i \frac{d\bar{h}_i}{dt} - \Delta v(Z_{SG} - Z_T)\frac{dP_s}{dt} + (1 - v_{i-1})(\bar{\rho}_{i-1}\bar{h}_{i-1} - \bar{\rho}_i \bar{h}_i)\frac{dZ_T}{dt}\right] = \dot{m}_{i-1}\bar{h}_{i-1} - \dot{m}_i \bar{h}_i + n\pi D_i \alpha_i \Delta v(Z_{SG} - Z_T)(\bar{T}_{w(i)} - \bar{T}_{s(i)}) \quad (36)$$

2.2.3.6 Steam valve model

The pressure of the steam generator and turbine are crucial factors that determine the mass flow rate of steam at the steam generator outlet. This can be regulated by the valve coefficient of the steam valve. The steam mass flow rate that is directed toward the turbine is modeled using:

$$m_{turbine} = K_c\sqrt{P_{SG} - P_{turbine}} \quad (37)$$

2.3 Solver Configuration

In the current research, we have select an appropriate solver algorithm for simulating the fluid flow and heat transfer using Python programing. We set convergence criteria for solution accuracy and we define residuals thresholds to control the iterative solver process. Finally, optimization of the solution settings for computational efficiency are carried out.

The HCSG mentioned three regions and comprising three sub-volumes. Consequently, a total of nine mass balance and nine energy equations must be formulated for the secondary system, while the primary system and tube metal's model require 18 energy equations.

To solve the secondary equations, $\dot{m}_{i-1}$ and $\dot{m}_i$ should be eliminated. Mass balance equations can be linked with inlet and outlet mass flow rate values. By utilizing this technique, the equation set for the secondary system can be expressed in the format presented in Table 2. The first nine equations in the table denote the energy equations for the secondary volumes, while equation ten represents the mass balance for the system. The mass balance equation is written in this form by combining all the mass balance equations.

Table 2: Equation set for the secondary side.

	Vol	Equation
Energy Balance for secondary	1	$a_{s1,1}\dot{P}_s + a_{s1,2}\dot{h}_1 = f_{s1}$
	2	$a_{s2,1}\dot{P}_s + a_{s2,2}\dot{h}_1 + a_{s2,3}\dot{h}_2 + a_{s2,4}\dot{Z}_s = f_{s2}$
	3	$a_{s3,1}\dot{P}_s + a_{s3,2}\dot{h}_1 + a_{s3,3}\dot{h}_2 + a_{s3,4}\dot{Z}_s = f_{s3}$
	4	$a_{s4,1}\dot{P}_s + a_{s4,2}\dot{h}_1 + a_{s4,3}\dot{h}_2 + a_{s4,4}\dot{\alpha}_1 + a_{s4,5}\dot{Z}_S = f_{s4}$
	5	$a_{s5,1}\dot{P}_s + a_{s5,2}\dot{h}_1 + a_{s5,3}\dot{h}_2 + a_{s5,4}\dot{\alpha}_1 + a_{s5,5}\dot{Z}_S + a_{s5,6}\dot{Z}_T + a_{s5,7}\dot{\alpha}_2 = f_{s5}$
	6	$a_{s6,1}\dot{P}_s + a_{s6,2}\dot{h}_1 + a_{s6,3}\dot{h}_2 + a_{s6,4}\dot{\alpha}_1 + a_{s6,5}\dot{Z}_S + a_{s6,6}\dot{Z}_T + a_{s6,7}\dot{\alpha}_2 = f_{s6}$
	7	$a_{s7,1}\dot{P}_s + a_{s7,2}\dot{h}_7 + a_{s7,3}\dot{h}_8 + a_{s7,4}\dot{h}_9 + a_{s7,5}\dot{Z}_T = f_{s7}$
	8	$a_{s8,1}\dot{P}_s + a_{s8,2}\dot{h}_8 + a_{s8,3}\dot{h}_9 + a_{s8,4}\dot{Z}_T = f_{s8}$
	9	$a_{s9,1}\dot{P}_s + a_{s9,2}\dot{h}_9 + a_{s9,3}\dot{Z}_T = f_{s9}$
Mass balance	10	$a_{s10,1}\dot{P}_s + a_{s10,2}\dot{h}_1 + a_{s10,3}\dot{h}_2 + a_{s10,4}\dot{\alpha}_1 + a_{s10,5}\dot{\alpha}_2 + a_{s10,6}\dot{h}_7 + a_{s10,7}\dot{h}_8 + a_{s10,8}\dot{h}_9 + a_{s10,9}\dot{Z}_s + a_{a10,10}\dot{Z}_T = f_{s10}$

This system of equations consists of ten derivatives and ten equations. Using Python symbolic packages like SymPy or MATLAB, an explicit term can be written for each derivative. With explicit derivative on the left-hand side and coefficients on the right, the set of ODEs can be solved using RK45 or Adams/BDF methods.

The secondary equations are coupled with tube metal and primary equations trough $\dot{Z}_S$ and $\dot{Z}_T$. Having known these parameters from the secondary equations, primary and tube metal equations can be calculated as it is in Table 3 and Table 4.

Table 3: Equation set for tube metals.

Vol	Equation
1	$\dot{T}_{w1} = (1/a_{w1,1}) * (f_{w1} - a_{w1,2}\dot{Z}_S)$
2	$\dot{T}_{w2} = (1/a_{w2,1}) * (f_{w2} - a_{w2,2}\dot{Z}_S)$
3	$\dot{T}_{w3} = (1/a_{w3,1}) * (f_{w3} - a_{w3,2}\dot{Z}_S)$
4	$\dot{T}_{w4} = (1/a_{w4,1}) * (f_{w4} - a_{w4,2}\dot{Z}_S - a_{w4,3}\dot{Z}_T)$
5	$\dot{T}_{w5} = (1/a_{w5,1}) * (f_{w5} - a_{w5,2}\dot{Z}_S - a_{w5,3}\dot{Z}_T)$
6	$\dot{T}_{w6} = (1/a_{w6,1}) * (f_{w6} - a_{w6,2}\dot{Z}_S - a_{w6,3}\dot{Z}_T)$
7	$\dot{T}_{w7} = (1/a_{w7,1}) * (f_{w7} - a_{w7,2}\dot{Z}_T)$
8	$\dot{T}_{w8} = (1/a_{w8,1}) * (f_{w8} - a_{w8,2}\dot{Z}_T)$
9	$\dot{T}_{w9} = (1/a_{w9,1}) * (f_{w9} - a_{w9,2}\dot{Z}_T)$

Table 4: Equation set for primary system.

Vol	Equation
1	$\dot{T}_{p1} = \left(f_{p1} - a_{p1,2}\dot{Z}_S\right)/a_{p1,1}$
2	$\dot{T}_{p2} = \left(f_{p2} - a_{p2,2}\dot{Z}_S\right)/a_{p2,1}$
3	$\dot{T}_{p3} = \left(f_{p3} - a_{p3,2}\dot{Z}_S\right)/a_{p3,1}$
4	$\dot{T}_{p4} = \left(f_{p4} - a_{p4,2}\dot{Z}_S - a_{p4,3}\dot{Z}_T\right)/a_{p4,1}$
5	$\dot{T}_{p5} = \left(f_{p5} - a_{p5,2}\dot{Z}_S - a_{p5,3}\dot{Z}_T\right)/a_{p5,1}$
6	$\dot{T}_{p6} = \left(f_{p6} - a_{p6,2}\dot{Z}_T\right)/a_{p6,1}$
7	$\dot{T}_{p7} = \left(f_{p7} - a_{p7,2}\dot{Z}_T\right)/a_{p7,1}$
8	$\dot{T}_{p8} = \left(f_{p8} - a_{p8,2}\dot{Z}_T\right)/a_{p8,1}$
9	$\dot{T}_{p9} = \left(f_{p9}\right)/a_{p9,1}$

The final form of the equations consists of 28 state variables. Adams/BDF method exists in SciPy, and is used for integrating the set of ODEs. This method utilizes automatic stiffness detection and switching (Hindmarsh, 1983; Petzold, 1983). The case study SG design data that are related to the current research is given by Table 5.

Table 5: The case study steam generator design data

Parameter	value	Unit
Number of steam generators per NPM	2	
Number of helical tubes per steam generator	690	
Number of helical tube columns	21	
Outer diameter of tubes	1.59	cm
Tube wall thickness	0.127	cm
Average length of tubes	24.2	m
Total heat transfer area	1665.57	m^2
Number of feedwater headers per steam generator	2	
Number of steam headers per steam generator	2	
Feedwater temperature	421.87	K
Main steam temperature range at nominal power	574.8-580.4	K
Outlet pressure	3.45	MPa
Plugging margin for SG tubes	10%	
Fouling factor	1.763×10^{-5}	m^2.K/W

3. Results and discussions

A RELAP5 model of the SG was previously developed in order to compare the steady state and transient results (Fakhraei et al., 2020; Fakhraei et al., 2021; Fakhrarei et al., 2021). This model is developed based on the design data of the case study SG (NuScale Power LLC, 2020). The shell side of the SG is composed of an annulus component containing 32 nodes. The heat transfer model of the vertical bundle with crossflow is employed for the primary system. To replicate the HCSG condition in the primary loop, the boundary condition for the system is carefully selected. A time-dependent junction 150 injects a mass flow rate of 587 kg/s into the system at the temperature of the core outlet, while the outlet of the primary

system is connected to a single junction that is linked to a time-dependent volume at the core inlet temperature. The tube side of the HCSG comprises a pipe with an equivalent cross-sectional area of the 1380 steam generator tubes. The pipe length is equal to the average tube length presented in Table 5, and it is divided into 32 calculational nodes. The vertical angle of the tubes is equal to the HCSG inclination angle, and the thermal-hydraulic parameters of the headers are chosen for the boundary condition of the secondary system.

3.1 Steady State Conditions

Table 6 presents the results of the models, which indicate excellent agreement with the reactor's design data and confirm the validity of the model. Additionally, the steady-state temperature profile of the primary and secondary sides are illustrated in Figure 9.

Table 6: Reference SG parameters and comparison with computational models in steady-state.

	Design data	RELAP5	Current model	Error*
Core outlet Temperature (K)	585.9	585.9	585.9	0%
Core inlet Temperature (K)	533.7	534.9	533.9	<0.03%
Feedwater inlet Temperature (K)	421.9	421.9	421.87	0%
Steam outlet temperature (K)	575 - 580	580.2	579.73	In range
Steam pressure (MPa)	3.45	3.45	3.45	<0.03%
Steam mass flow rate (kg/s)	67	67	67	0%
Primary mass flow rate (kg/s)	587	587	587	0%

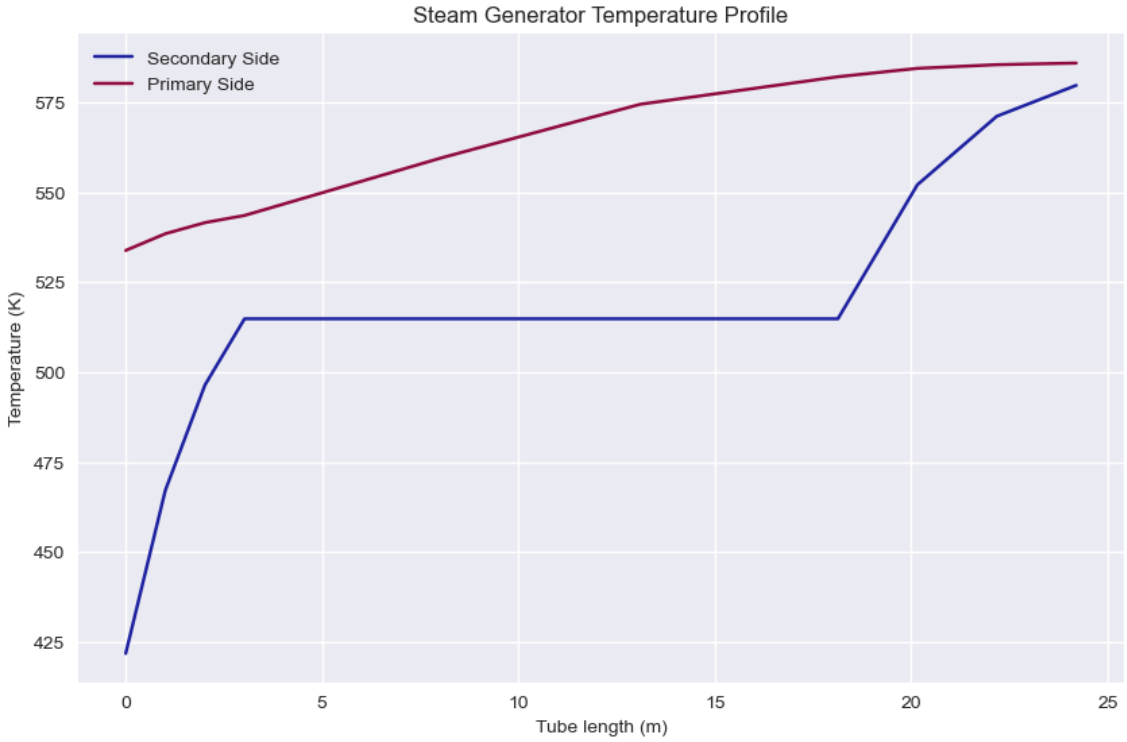

Figure 2: Steam generator temperature profile for primary and secondary side based on developed model.

3.2 Transient Performance of the Model

Inputs of the steam generator model comprised several parameters. These parameters include core outlet temperature and its flow rate, feedwater temperature and flow ratethat are mentioned in Table 5 and Table 6. Conservative assumptions are adopted for performance evaluation, such as maximum core temperature outlet to the primary part of SGs.

3.2.1 Ramp Change of Feedwater Flow Rate

A 5% reduction in feedwater mass flow was introduced at 100 s and continued until the end of the simulation. The resulting pressure variation during the transient is presented in Figure 10, which demonstrates a decrease in pressure due to the ramp feedwater reduction. Accurate calculation of the primary side outlet temperature is crucial as its variations can affect core inlet temperature. The results from the two codes are compared in Figure 11, which reveals a similar trend of changes and the same final temperature change for both codes.

Figure 12 provides the effect of the ramp 5% decrease in feedwater flow rate on the steam temperature, revealing a consequent rise in steam temperature that is consistent with anticipated behavior. However, although the trend for steam temperature remains consistent across the two methods employed, minor less than 2 degree differences in the final values are observed. The specific heat capacity of the superheat section of the case study SG is significantly lower than that of the primary and other SG sections. As a result, output temperature becomes much more susceptible to minor differences. Consequently, even slight differences in the length of the superheat section can lead to temperature differences between RELAP5 and the mathematical model. This fact accounts for the observed temperature difference in Figure 12.

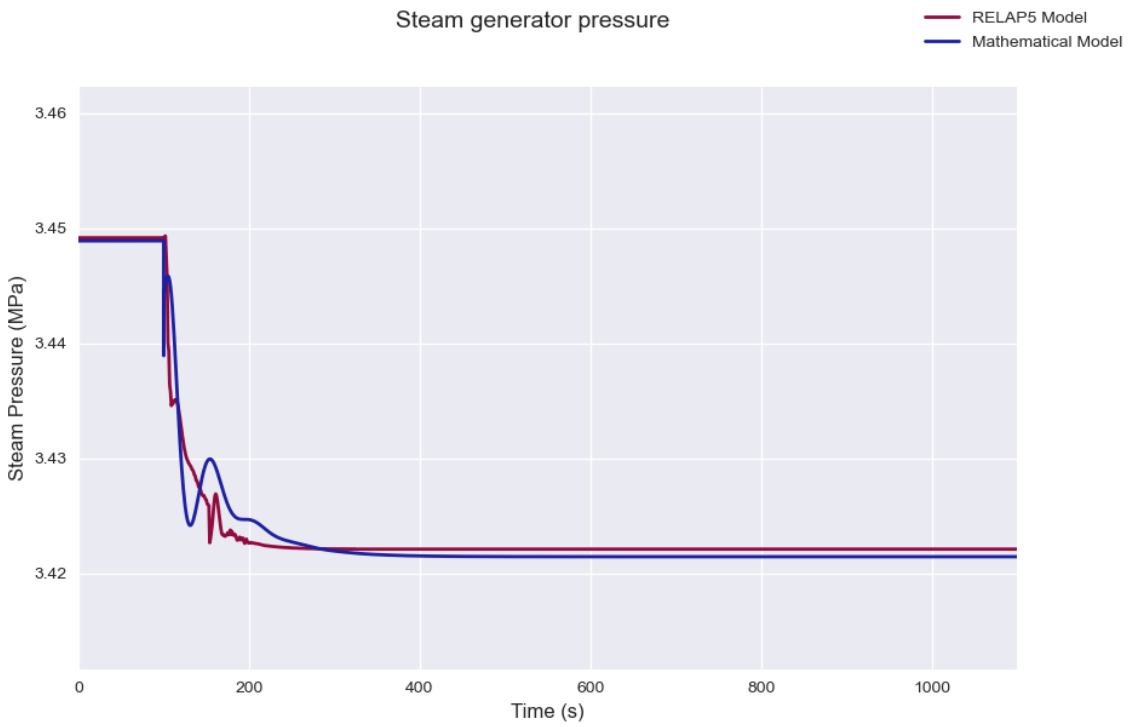

Figure 3: Secondary side pressure response to the 5% decrease in feedwater flow rate.

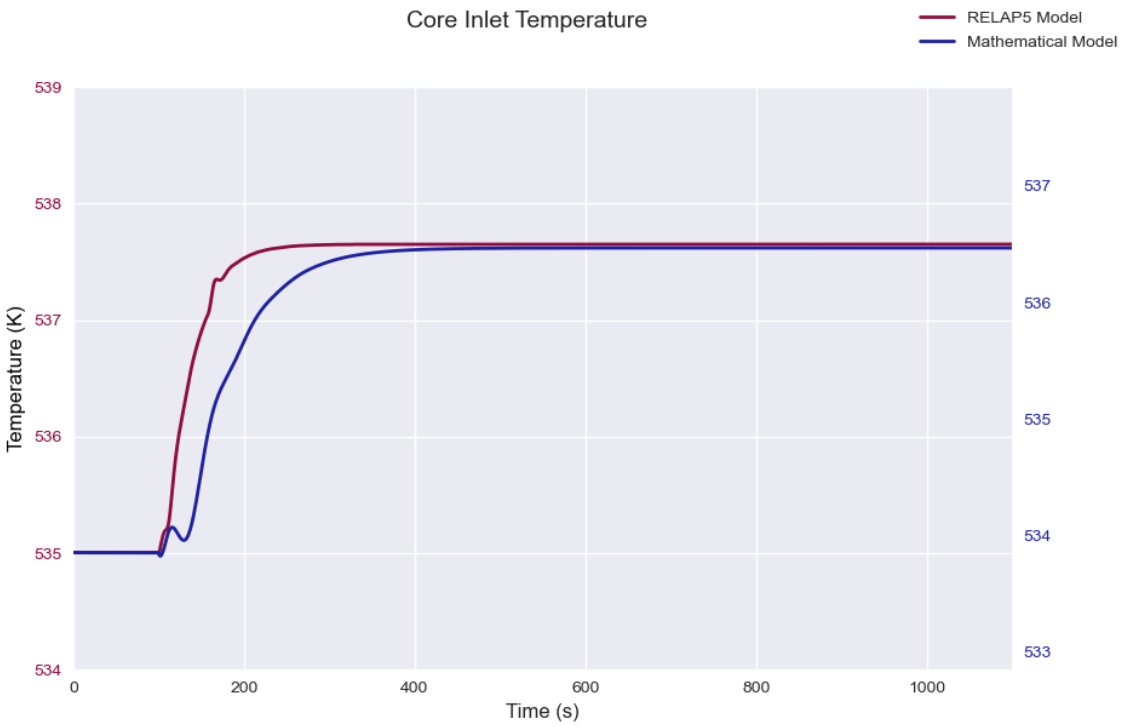

Figure 4: Primary side outlet temperature response to the 5% decrease in feedwater flow rate.

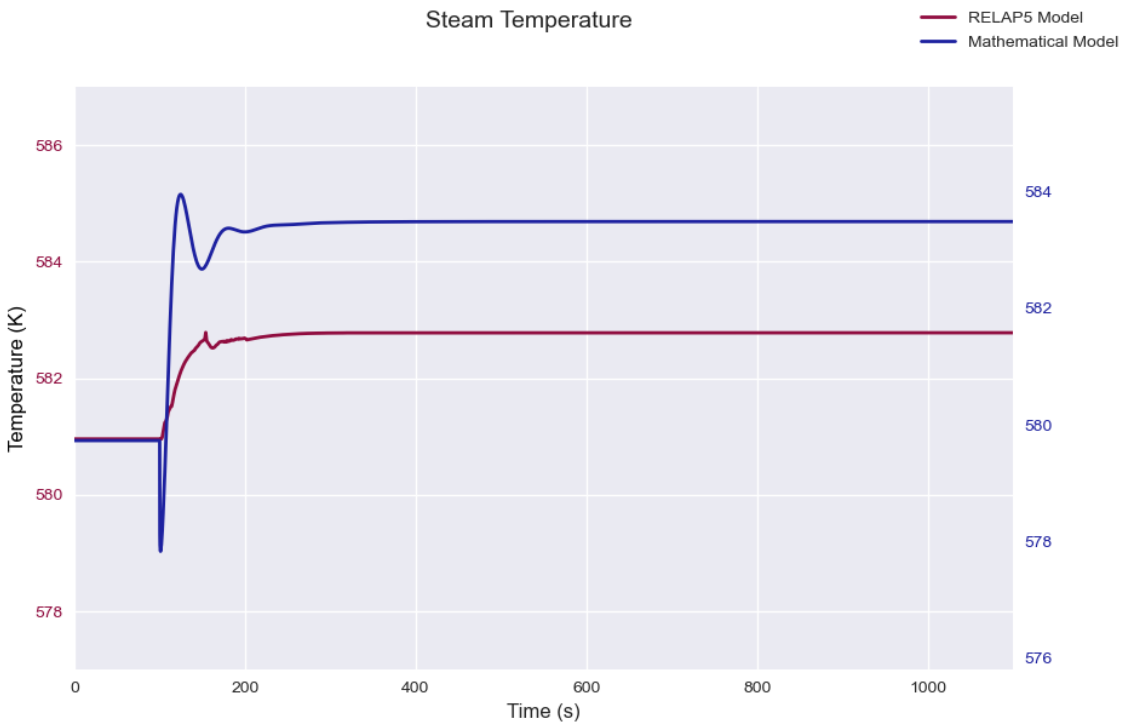

Figure 5: Secondary side inlet temperature response to the 5% decrease in feedwater flow rate.

3.2.2 Step Change in the Primary Flow Rate

In this scenario, the primary system undergoes a ramp change of the mass flow rate increases from 578 kg/s to 616.35 kg/s. This represents a 5% increase in the primary flow rate. The step change of flow rate starts at time t=100s.

The increase in mass flow leads to a corresponding increase in energy deposition within the secondary system, and eventually leads to an increase in velocity and heat transfer coefficients within the primary side, which in turn contribute to a greater heat transfer to the secondary side.

The pressure of the secondary side of the SG is shown in Figure 13. An increase in energy that the primary system receives leads to a corresponding increase in pressure within the SG. However, as the temperature rises and the outlet mass flow rate rebalances, the pressure gradually decreases back to its nominal value.

Figure 14 shows the temperature rise observed in the SG outlet flow moving toward the core. This temperature increase results in a constant secondary flow rate with a constant heat removal capacity. The current CFD and RELAP5 code calculated identical values of temperature change, indicating the reliability and consistency of the CFD. Figure 15 also shows the outlet steam temperature of the SG response to 5% step increase of the primary flow rate. After a decrease caused by the pressure peak and more flow discharge from the primary side, the steam temperature reaches a new set-point.

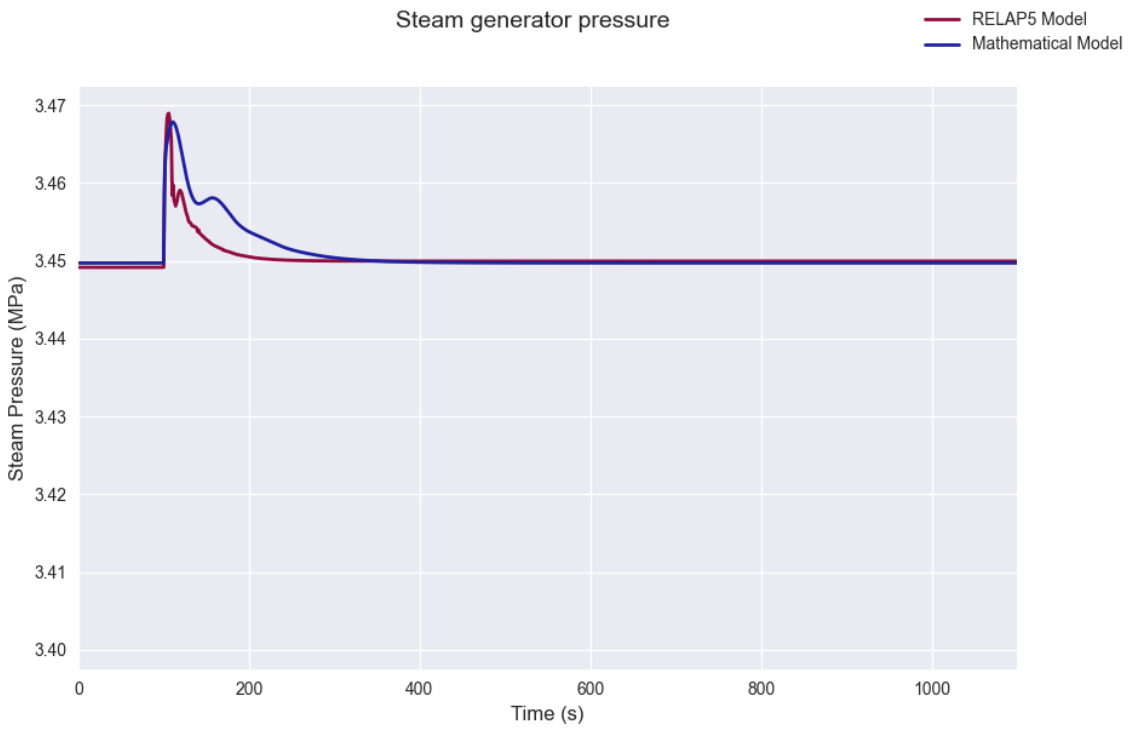

Figure 6: Secondary side pressure response to 5% step increase in primary mass flow rate.

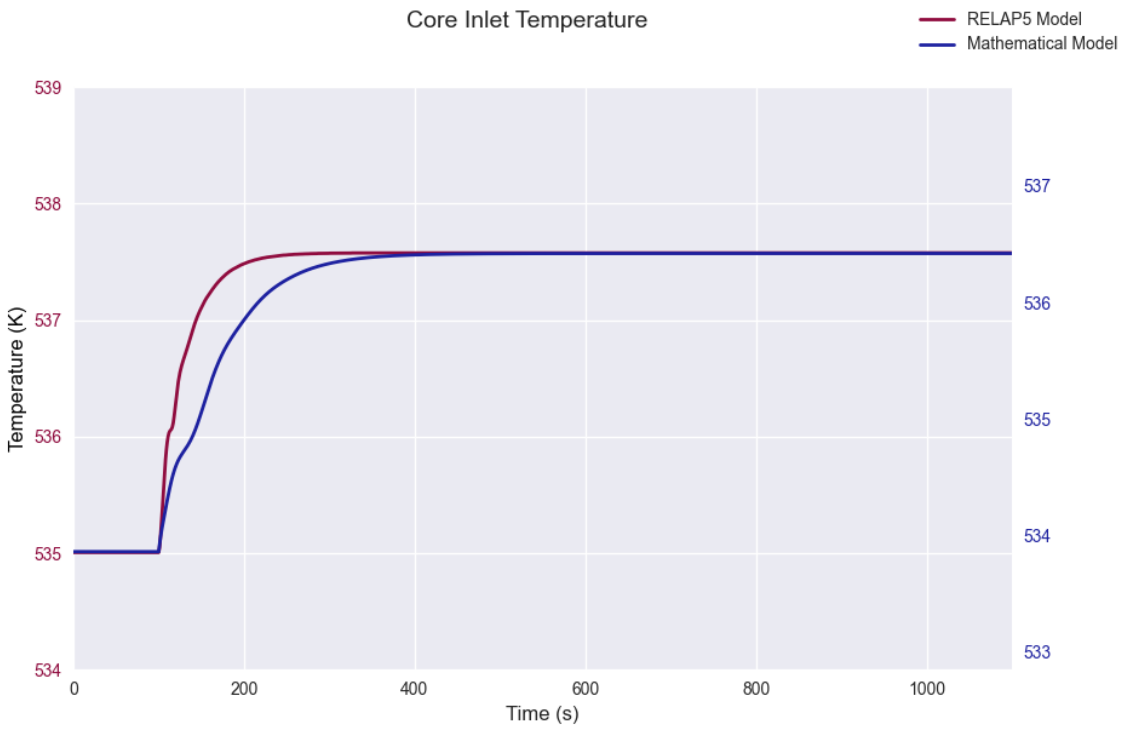

Figure 7: Primary inlet temperature or the SG outlet temperature into the primary side response to 5% ramp increase in primary mass flow rate.

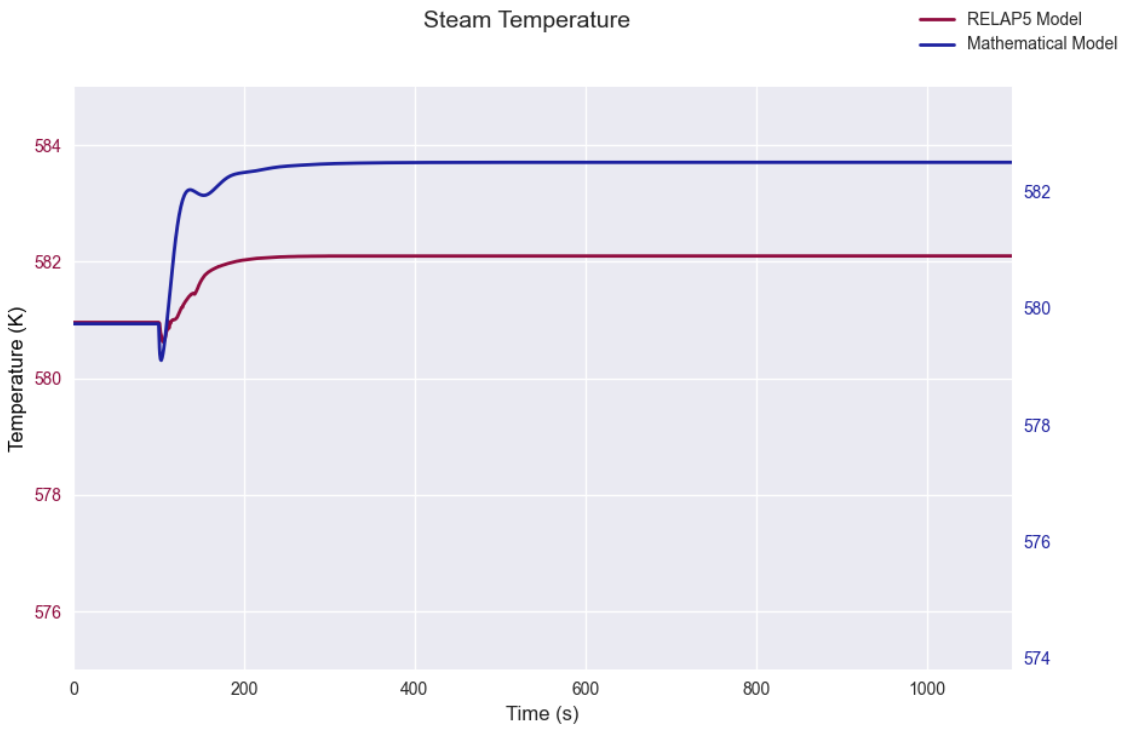

Figure 8: The outlet steam temperature response to 5% step increase in primary mass flow rate.

3.2.3 Step Change in the Feedwater Temperature

To assess the performance of the developed model, another scenario is considered where the feedwater temperature is decreased by 10 degrees, or a 10-degree step decrease in the feedwater temperature. The resulting fluctuation in the secondary side pressure is observed, as shown in Figure 16. After the system reaches a new temperature equilibrium, the pressure in the secondary system reaches a minor less equilibrium set-point.

Figure 17 demonstrates that a decrease in feedwater temperature results in a reduction of primary side outlet temperature. Both methods predict a temperature reduction of nearly 1K for the primary side outlet as the secondary temperature decreases by 10 K.

Figure 18 illustrates the steam temperature in the scenario under consideration. Most of the primary heat is allocated to phase change in the secondary, which is a dominant part of heat transfer in the secondary system. On the other hand, a feedwater temperature decrease leads to more efficient heat transfer from the primary in the subcooled region. Therefore, the overall effects of feedwater temperature decrease would be negligible on steam temperature, as shown in Figure 18. It is also worth noting that the performance of both models for the prediction of steam temperature is similar.

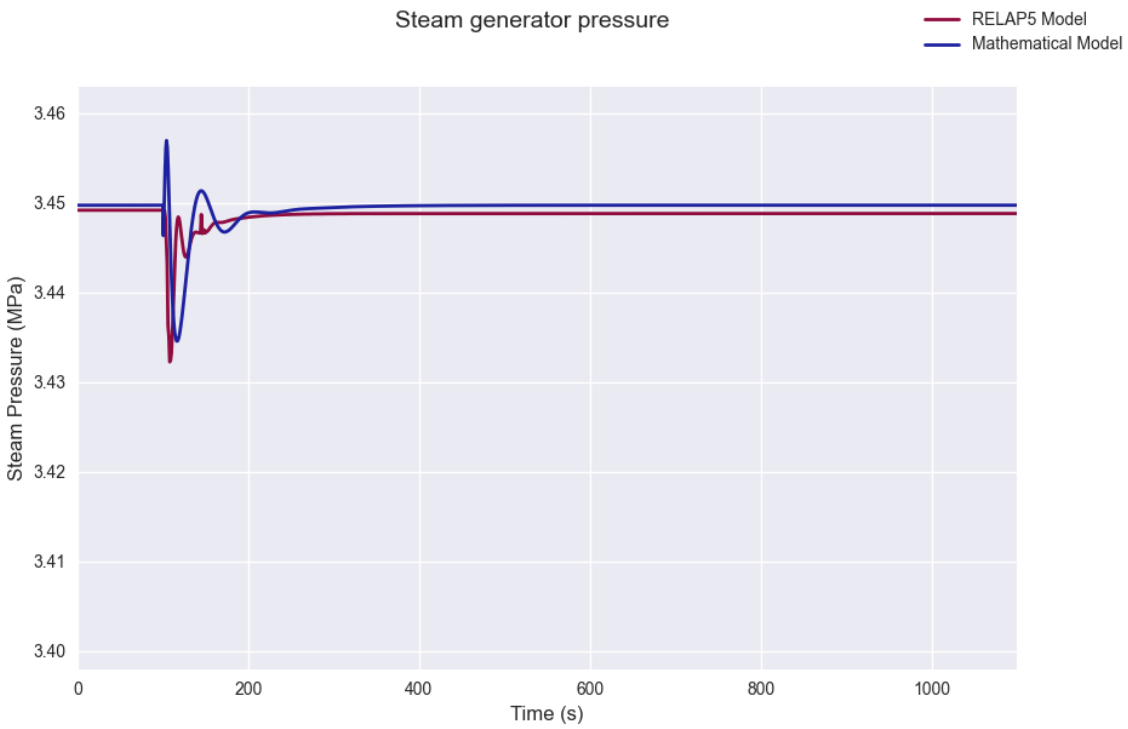

Figure 9: Secondary side pressure response to 10 degrees decrease in the feedwater temperature.

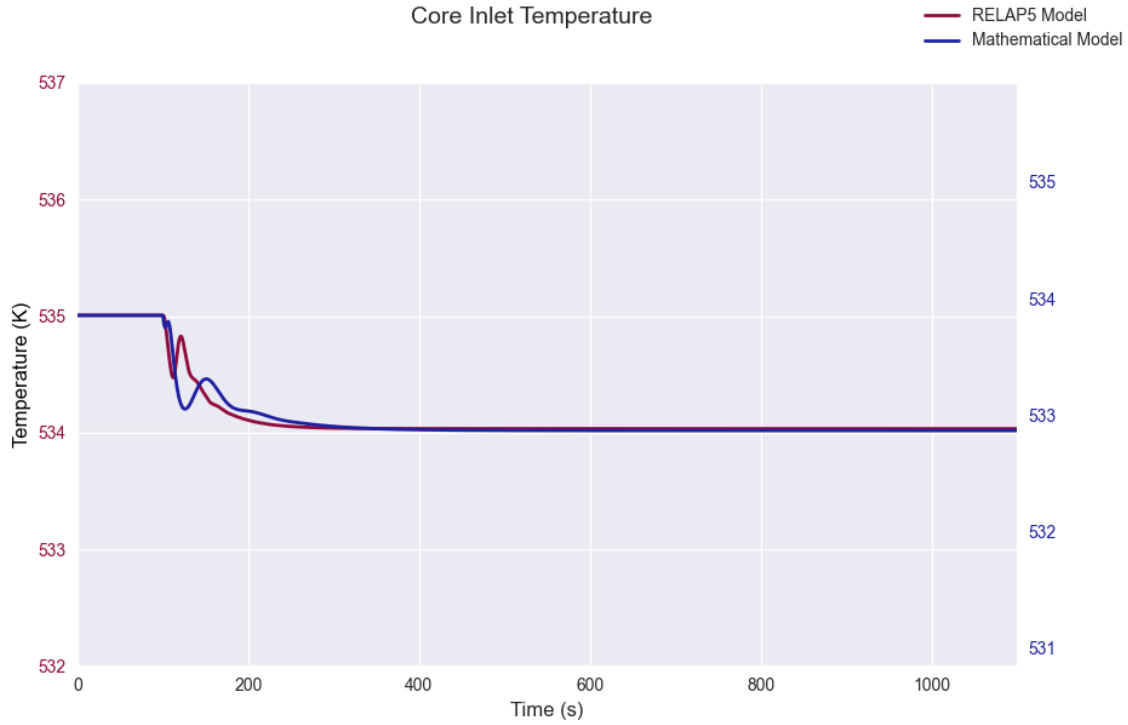

Figure 10: Primary side temperature response to 10 degrees decrease in secondary feedwater temperature.

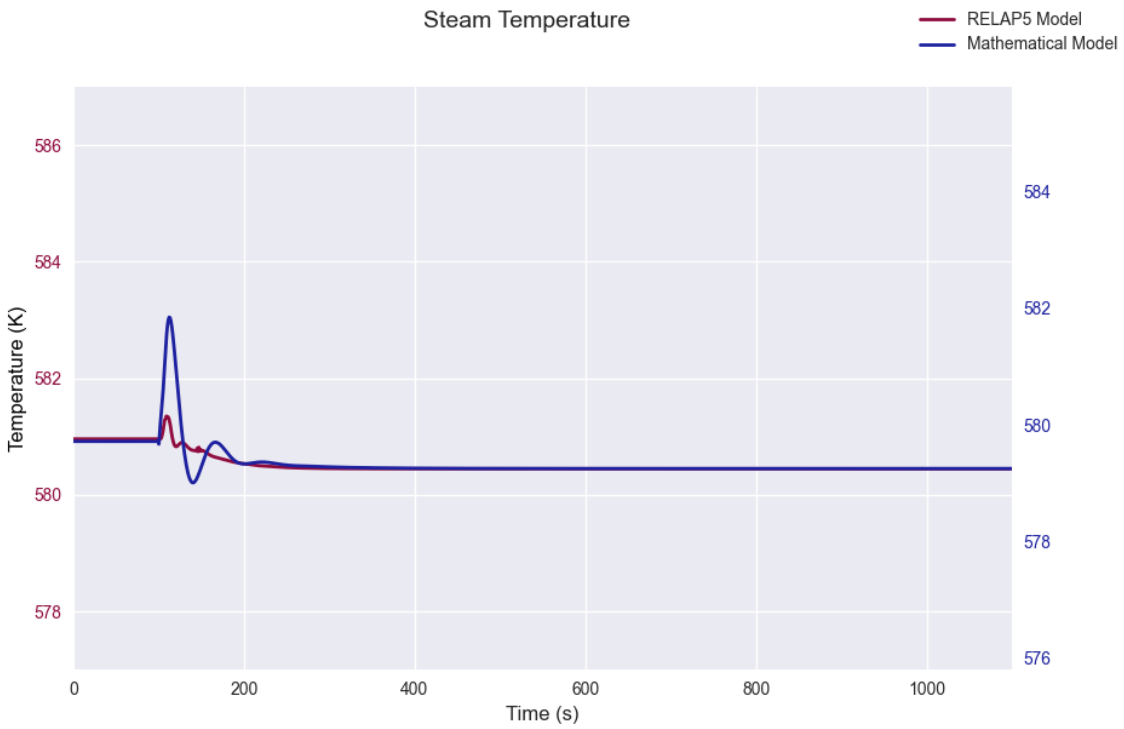

Figure 11: The steam temperature response to 10 degrees reduction in the feedwater temperature.

3.2.4 Step Change in the Core Outlet Temperature

In this scenario, a step change of two degrees in the primary side inlet temperature of the SG is considered, which is approximately equivalent to a 6.1 MW increase in the energy generation of the core. As a result of this energy increase, pressure peaks are observed in the secondary side during the first few seconds, as depicted in Figure 19.

Some amount of added energy to the system is transferred to the secondary and causes the steam temperature to rise. The amount of temperature increase is shown in Figure 21. The rest of the energy not transported to the secondary causes a temperature increase in outlet flow. According to the results presented in Figure 20, from the 2K increase of the input, slightly more than 1K was transported directly out of the system by primary outlet flow.

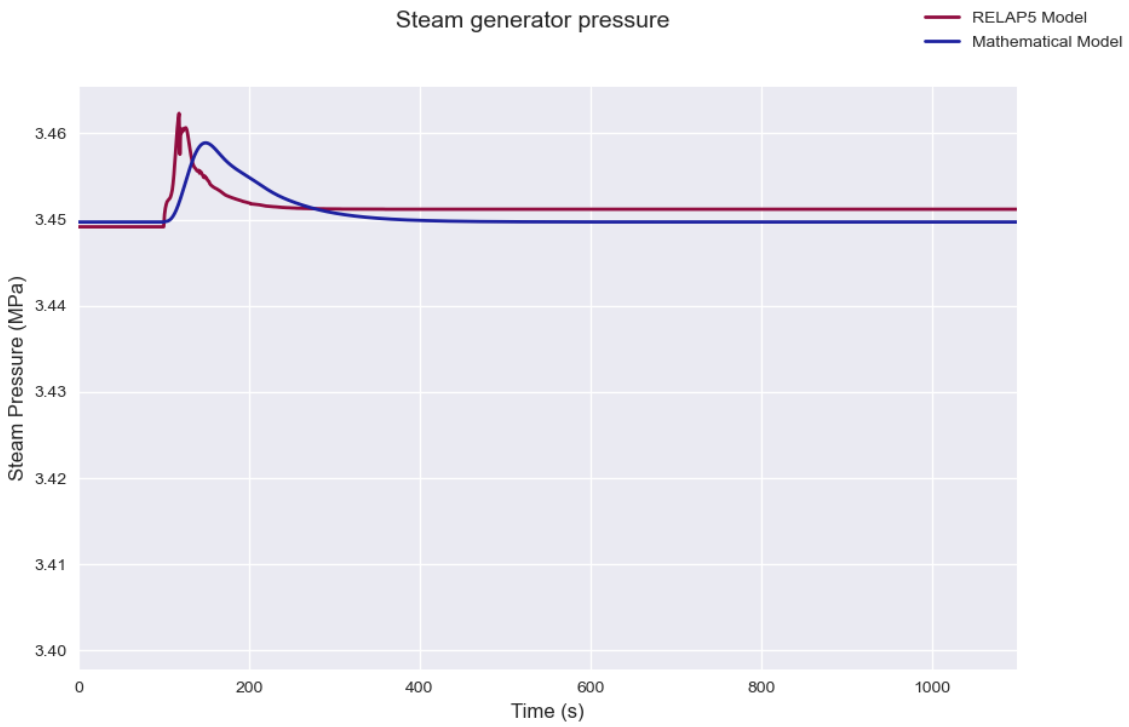

Figure 12: Secondary side pressure response to 2 degrees increase in outlet primary side temperature that enters the SG

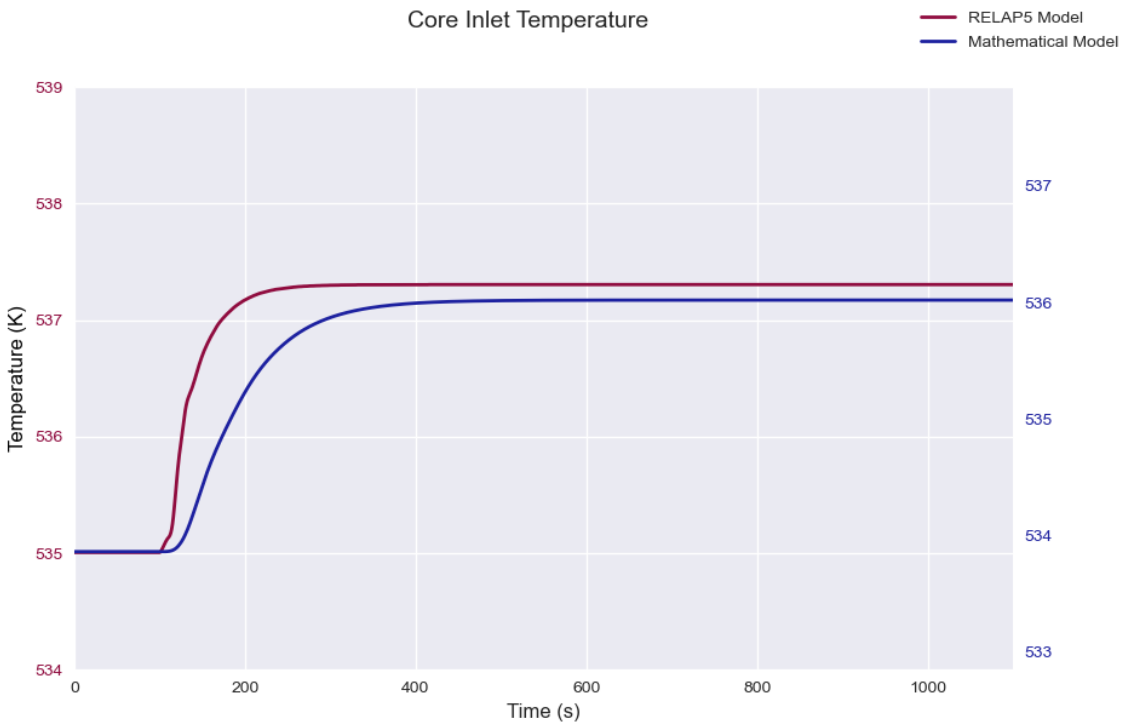

Figure 13: Primary side temperature response to 2 degrees increase in primary inlet temperature.

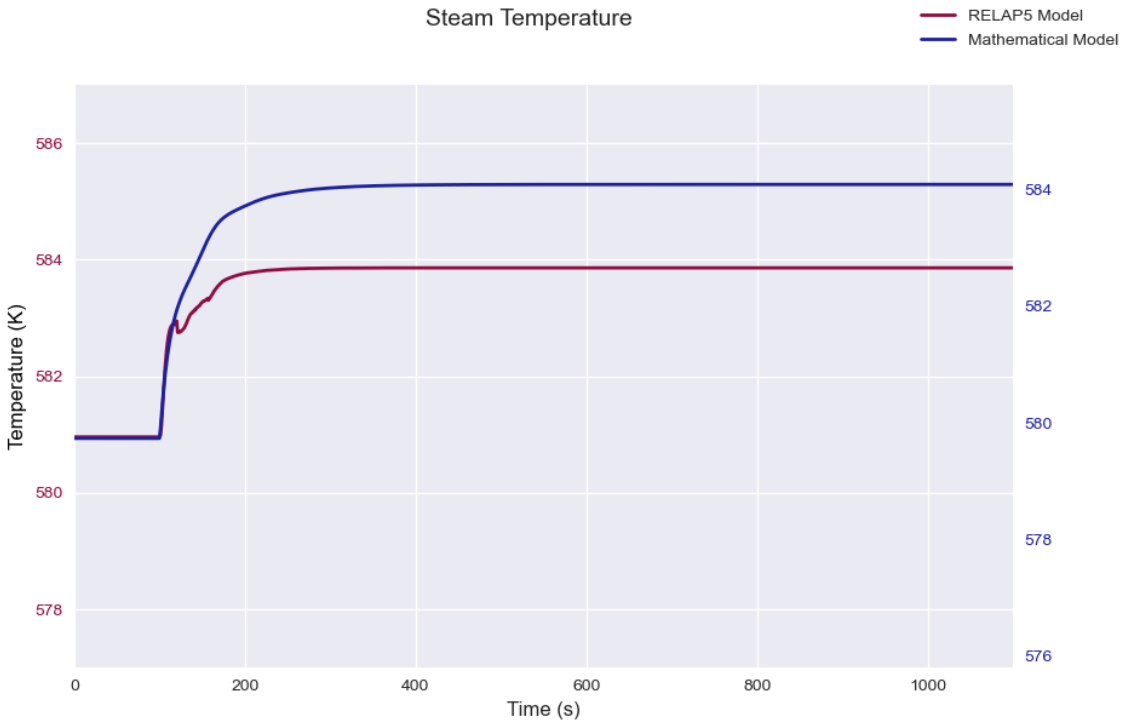

Figure 14: Secondary side temperature response to 2 degrees increase in primary inlet temperature.

4. Conclusion

In this research, a multi-node moveable boundary model is developed for a typical counter current helically coiled SG. The secondary side of SG is divided into three regions and linked with primary side and the tube metal equations. Each region is modelled using its own formulation and heat transfer coefficients. Steam generator performance of the case study module is simulated using this technique. Calculated results show a good agreement between the published design data and the developed CFD simulations in the steady state case. The model's response to several transients of the SG inputs are calculated and compared with the RELAP5 code. It is observed that the trend of transient responses was similar in all cases. The change in final values for pressure and primary outlet temperature was in good agreement between the developed CFD and RELAP5. Due to the different nature of equations between RELAP5 and current CDF as well as the solving methods, there was a minor difference between the results for steam temperature, however, the overall behaviors were identical.

Python programming allows creation of fine simulations to analyze the performance of SGs under varying input conditions. Through the use of numerical methods and differential equations solvers, we could simulate heat transfer processes, fluid flow dynamics, and pressure distributions within the SG. These simulations provide valuable insights into SG behavior and aid in optimizing design parameters. Python's data analysis and visualization libraries, such as Pandas and Matplotlib, enable us to analyze and interpret large sets of SG data. Furthermore, visual representations, such as graphs and plots, help in presenting the obtained transient data. Using libraries like Tkinter or PyQt, we can create intuitive graphical user interfaces (GUIs) that enable users to sketch parameters, perform calculations, and visualize results.

References

[1] Ansarifar, G., 2016. Control of the nuclear steam generators using adaptive dynamic sliding mode method based on the nonlinear model. Annals of Nuclear Energy 88, 280-300.

[2] Arda, S.E., Holbert, K.E., 2015. A dynamic model of a passively cooled small modular reactor for controller design purposes. Nuclear Engineering and Design 289, 218-230.

[3] Arda, S.E., Holbert, K.E., 2016. Nonlinear dynamic modeling and simulation of a passively cooled small modular reactor. Progress in Nuclear Energy 91, 116-131.

[4] Atomenergoproekt, 2015. Final safety analysis report of BNPP's VVER-1000 reactor, Moscow.

[5] Berry, G., 1983. Model of a once-through steam generator with moving boundaries and a variable number of nodes. Argonne National Lab., IL (USA).

[6] Chen, A.T.-l., 1976. A DIGITAL SIMULATION FOR NUCLEAR ONCE-THROUGH STEAM GENERATORS. The University of Tennessee.

[7] Chen, J.C., 1966. Correlation for boiling heat transfer to saturated fluids in convective flow. Industrial & engineering chemistry process design and development 5, 322-329.

[8] Fakhraei, A., Faghihi, F., Rabiee, A., Safarinia, M., 2021. Coolant flow rate instability during extended station blackout accident in NuScale SMR: Two approaches for improving flow stability. Progress in Nuclear Energy 131, 103602.

[9] Fakhrarei, A., Faghihi, F., Dast-Belaraki, M., 2021. Theoretical study on the Passively Decay Heat Removal System and the primary loop flow rate of NuScale SMR. Annals of Nuclear Energy 161, 108420.

[10] Gnielinski, V., 1976. New equations for heat and mass transfer in turbulent pipe and channel flow. Int. Chem. Eng. 16, 359-368.

[11] Hindmarsh, A.C., 1983. ODEPACK: A systemized collection of ODE solvers. Scientific computing, 55-64.

[12] Höld, A., 1990. UTSG-2—A theoretical model describing the transient behavior of a pressurized water reactor natural-circulation U-tube steam generator. Nuclear technology 90, 98-118.

[13] Hu, K., Yuan, J., 2008. On switching H∞ controllers for nuclear steam generator water level: a multiple parameter-dependent Lyapunov functions approach. Annals of Nuclear Energy 35, 1857-1863.

[14] Irving, E., Miossec, C., Tassart, J., 1980. 32a. Towards efficient full automatic operation of the PWR steam generator with water level adaptive control, Boiler dynamics and control in nuclear power stations 2. Thomas Telford Publishing, pp. 309-329.
[15] Jensen, J.M., Tummescheit, H., 2002. Moving boundary models for dynamic simulations of two-phase flows, Proc. of the 2nd int. modelica conference. Oberpfaffhenhofen Germary.
[16] Kerlin, T., 1976. HTGR steam generator modeling. Oak Ridge National Lab.
[17] Kothare, M.V., Mettler, B., Morari, M., Bendotti, P., Falinower, C.-M., 2000. Level control in the steam generator of a nuclear power plant. IEEE transactions on control systems technology 8, 55-69.
[18] Lee, J., Akcasu, Z., Duderstadt, J., Crump, M., Van Tuyle, G., Meernik, P., Fortino, R., Feng, Y., 1980. Review of transient modeling of steam generator units in nuclear power plants. Michigan Univ., Ann Arbor (USA). Dept. of Nuclear Engineering.
[19] Lee, S.K., Chang, S.H., 2008. Experimental study of post-dryout with R-134a upward flow in smooth tube and rifled tubes. International Journal of Heat and Mass Transfer 51, 3153-3163.
[20] Lewis, E.E., 1977. Nuclear power reactor safety.
[21] Mitchell, M., 1998. An introduction to genetic algorithms. MIT press.
[22] Munasinghe, S.R., Kim, M.-S., Lee, J.-J., 2005. Adaptive neurofuzzy controller to regulate UTSG water level in nuclear power plants. IEEE Transactions on Nuclear Science 52, 421-429.
[23] NuScale Power LLC, 2020. NuScale Standard Plant Design Certification Application. U.S. Nuclear Regulatory Commission (NRC).
[24] Patankar, S.V., 2018. Numerical heat transfer and fluid flow. CRC press.
[25] Petzold, L., 1983. Automatic selection of methods for solving stiff and nonstiff systems of ordinary differential equations. SIAM journal on scientific and statistical computing 4, 136-148.
[26] Secker, P., Gilbert, J., 1975. Status of CHAP: composite HTGR analysis program. Los Alamos Scientific Lab.
[27] Todreas, N.E., Kazimi, M.S., 2012. Nuclear systems: thermal hydraulic fundamentals. CRC press.
[28] Tzanos, C.P., 1988a. A movable boundary model for once-through steam generator analysis. Nuclear Technology 82, 5-17.
[29] Tzanos, C.P., 1988b. A semianalytic method for the solution of the steady-state steam generator equations. Nuclear Technology 80, 380-391.
[30] Wan, J., Wu, S., Nuerlan, A., Zhao, F., 2017. Dynamic modeling of AP1000 steam generator for control system design and simulation. Annals of Nuclear Energy 109, 648-657.
[31] Westinghouse, 2011. AP1000 Design Control Document. NRC, https://www.nrc.gov/docs/ML1117/ML11171A500.html.
[32] Wu, Y., Liu, B., Zhang, H., Guo, J., Li, F., 2022. A movable boundary model for helical coiled once-through steam generator using preconditioned JFNK method. International Journal of Advanced Nuclear Reactor Design and Technology 4, 1-8.
[33] Wu, Y., Liu, B., Zhang, H., Zhu, K., Kong, B., Guo, J., Li, F., 2021. Accuracy and efficient solution of helical coiled once-through steam generator model using JFNK method. Annals of Nuclear Energy 159, 108290.
[34] Yang, X.-S., 2020. Nature-inspired optimization algorithms. Academic Press.
[35] Zhang, Y., Wang, D., Lin, J., Hao, J., 2017. Development of a computer code for thermal–hydraulic design and analysis of helically coiled tube once-through steam generator. Nuclear Engineering and Technology 49, 1388-1395.
[36] Žukauskas, A., 1972. Heat transfer from tubes in crossflow, Advances in heat transfer. Elsevier, pp. 93-160.